



Experimental characterisation of the local mechanical behaviour of cellulose fibres: an *in-situ* micro-profilometry approach

S. Maraghechi · E. Bosco · A. S. J. Suiker ·
J. P. M. Hoefnagels

Received: 21 October 2022 / Accepted: 15 March 2023 / Published online: 31 March 2023
© The Author(s) 2023

Abstract The accurate mechanical characterisation of fibres of micrometric length is a challenging task, especially in the case of organically-formed fibres that naturally exhibit considerable irregularities along the longitudinal fibre direction. The present paper proposes a novel experimental methodology for the evaluation of the *local* mechanical behaviour of organically-formed (aged and unaged) and regenerated cellulose fibres, which is based on *in-situ* micro-tensile testing combined with optical profilometry. In order to accurately determine the cross-sectional area profile of a cellulose fibre specimen, optical profilometry is performed both at the top and bottom surfaces of the fibre. The evolution of the local stress at specific fibre locations is next determined from the force value recorded during the tensile test and the local cross-sectional area. An accurate measurement of the corresponding local strain is obtained by using Global Digital Height Correlation (GDHC), thus resulting in multiple, local stress–strain curves per fibre, from which local tensile strengths, elastic

moduli, and strains at fracture can be deduced. Since the variations in the geometrical and material properties within an individual fibre are comparable to those observed across fibres, the proposed methodology is able to attain statistically representative measurement data from just one, or a small number of fibre samples. This makes the experimental methodology very suitable for the mechanical analysis of fibres taken from valuable and historical objects, for which typically a limited number of samples is available. It is further demonstrated that the accuracy of the measurement data obtained by the present, local measuring technique may be significantly higher than for a common, global measuring technique, since possible errors induced by fibre slip at the grip surfaces are avoided.

Keywords Digital image correlation · Cellulose · Natural micrometric fibres · Fibre tensile testing · Optical profilometry

Introduction

The macro-scale mechanical response of fibrous materials, such as paper or textiles, is governed by complex mechanisms originating from the fibre level. A thorough understanding of the material behaviour at the macroscopic level thus requires the mechanical characterisation of single fibres. Atomic force microscopy-based nanoindentation (Ganser et al.

S. Maraghechi · E. Bosco (✉) · A. S. J. Suiker
Department of the Built Environment, Applied Mechanics,
Eindhoven University of Technology, P.O. Box 513,
5600 MB Eindhoven, The Netherlands
e-mail: e.bosco@tue.nl

J. P. M. Hoefnagels
Department of Mechanical Engineering, Eindhoven
University of Technology, P.O. Box 513,
5600 MB Eindhoven, The Netherlands

2014; Czibula et al. 2020) and Brillouin spectroscopy (Elsayad et al. 2020) have been proposed in the literature as indirect techniques to measure the elastic modulus; however, they do not enable the characterisation of the fibre's plastic, micro-damage and fracture behaviour. To assess the full mechanical behaviour, i.e., the full stress-strain curve, the mechanical loading is commonly applied by means of a standard uniaxial tensile test (El-Hosseiny and Page 1975; Kappil et al. 1995; Mott et al. 1996; Kouko et al. 2019; Kompella and Lambros 2002; Burgert et al. 2003; Eder et al. 2008; Jajcinovic et al. 2016, 2018), whereby a *global* displacement measurement provides the evolution of the average fibre strain, and the corresponding effective stress in the fibre is calculated from the cross-sectional area measured at *one specific location* within the fibre. With this procedure, various types of fibres have been mechanically characterized, including flax fibres (Bos and Donald 1999), hemp fibres (Baley 2002), organically-formed cellulose fibres (El-Hosseiny and Page 1975; Burgert et al. 2003) and regenerated cellulose fibres (Chen 2015; Adusumali et al. 2006; Adusumalli et al. 2006; Gindl et al. 2006, 2008).

Although a standard uniaxial tensile test is robust and relatively straightforward to perform, the accuracy and interpretation of the measured mechanical response require careful attention, especially in the case of organically-formed fibres, such as cellulose-based paper fibres. Organically-formed fibres are characterized by significant geometric irregularities in the longitudinal fibre direction, as a result of which the fibre mechanical response and physical properties may be expected to vary along the fibre length (Ganser et al. 2014; Czibula et al. 2020). Fig. 1 shows Scanning Electron Micrograph (SEM) images of an organically-formed cellulose (paper) fibre (Fig. 1a) and a regenerated cellulose (viscose) fibre (Fig. 1b), which indeed illustrates that the shape of the paper fibre is rather irregular, while that of the viscose fibre is more or less uniform. Due to variations in growth and extraction condition, the material properties and physical behaviour of organically-formed fibres may also vary from fibre to fibre (Mohanty et al. 2000), which requires a relatively large number of tests for obtaining statistically representative data from measurements of the overall, global fibre response.

In the present work, a novel, systematic experimental methodology based on *in-situ* tensile testing

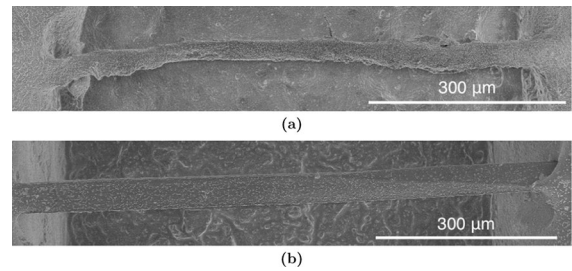


Fig. 1 Scanning electron micrograph of **a** an organically-formed cellulose fibre (paper) with significant shape irregularities along the longitudinal direction, and **b** a regenerated cellulose fibre (viscose), characterized by a flat, rectangular cross-section and limited shape variations

combined with Optical Profilometry is elaborated, which enables an efficient and accurate characterisation of the mechanical response of individual fibres of micrometric length. The distinctive features of the proposed methodology are as follows. (i) The stresses and strains are evaluated *locally* along the longitudinal fibre direction, utilising an accurate, automatized height profile acquisition. (ii) The *local stresses* are determined through the evaluation of the cross-sectional area of the fibre along its length, applying two-sided, high-magnification optical profilometry of the fibre prior to tensile testing, and incrementally recording the applied load. (iii) The *local strains* are obtained through an accurate high-magnification 3D surface evaluation at multiple locations along the longitudinal direction of the fibre, in combination with a specific type of Digital Image Correlation (DIC) named Global Digital Height Correlation (GDHC), which is performed on profilometry images.

Under the plausible assumption that the material and morphological variations within a single fibre (i.e., intra-fibre variations) are comparable to those between different fibres (i.e., inter-fibre variations), the local stresses and strains measured on a single fibre enable to deduce statistically representative material data (elastic modulus, ultimate tensile strength, strain at fracture) from a relatively low number of tensile tests. The proposed methodology is validated on a viscose fibre that is characterized by a regular shape (see Fig. 1b), and organically-formed cellulose paper fibres that exhibit considerable intra-fibre shape irregularities (see Fig. 1a). For the testing of organically-formed cellulose fibres, six samples have been extracted from a Whatman No. 1 filter

paper sheet, and two samples have been taken from a historic paper document dated 1834. Although the focus of the present study is on cellulose fibres, the proposed methodology is generic and can be applied to arbitrary fibres of micrometric length.

It is emphasised that the possibility of obtaining relevant statistical information from only a few tensile tests makes the proposed experimental method particularly relevant for the analysis of cultural heritage materials, for which typically a low number of fibre samples can be extracted from the considered art object, e.g., paper fibres from ancient books or cotton/linen fibres from valuable and historical canvas paintings. The mechanical characteristics measured from the combined micro-tensile testing and optical profilometry approach provide detailed insight into the local material behaviour of fibres, and can be used as input for degradation models and complementary experimental studies of historical materials, such as historical paper (Zou et al. 1994, 1996; Emsley et al. 2000; Tétreault et al. 2013; Čabalová et al. 2017; Parsa Sadr et al. 2022; Maraghechi et al. 2023) or canvas (Seves et al. 2000; Kavkler and Demšar 2011; Oriola et al. 2014; Nechyporchuk et al. 2017).

This paper is organized as follows. Section Methodology presents the testing methodology, including the sample preparation procedure, the optical profilometry method to obtain cross-sectional area measurements, and the strain evaluation procedure as performed via GDHC. The results of the tensile experiments on three different cellulose-based fibres (viscose fibre, fibres from Whatman filter paper and fibres from a historic paper document) are discussed and compared in Section Results and Discussion. The main conclusions are finally presented in Section Conclusions.

Methodology

The mechanical response of individual, cellulose-based fibres was measured by means of the following experimental procedure. First, a fibre was carefully extracted from the actual source and attached to a carrier frame, followed by an accurate measurement of the cross-sectional area profile along the fibre length. Next, a speckle pattern was applied on the top surface of the fibre, from which an accurate measurement of the local strains was obtained by using Global Digital

Height Correlation (GDHC). Finally, uniaxial tensile tests were performed, whereby the local measurement data of fibre samples were used for constructing stress–strain curves. The above experimental steps are successively described in subsections Sample preparation to Global Digital Height Correlation analysis below.

Sample preparation

The preparation of individual, cellulose-based fibres for tensile testing generally is a challenging task, since cellulose fibres are typically fragile and have a small size with a thickness of a few tens of micrometres and a length of a few hundreds of micrometres. Two types of cellulose-based fibres were considered in the current experimental procedure, namely *organically-formed* cellulose fibres and *regenerated* viscose fibres. Organically-formed cellulose fibres are characterized by a hierarchical micro-structure consisting of micro-fibrils and fibrils embedded in a matrix of hemicellulose and lignin. Conversely, regenerated cellulosic fibres, such as viscose, are extruded from dissolved and purified organic cellulose fibres and therefore are more homogeneous in terms of shape and mechanical properties.

The organically-formed cellulose fibres were extracted from a macroscopic paper sheet, by making small tears to expose the fibres. Alternatively, fibres could have been extracted by attaching and rapidly removing a piece of adhesive tape on the paper sheet. The exposed fibres were pulled out using a pair of fine-tip tweezers. This process was performed underneath a ZEISS™, Stemi 2000-C stereo microscope. The organically-formed cellulose fibres were extracted from two different macroscopic paper samples: a Whatman No. 1 filter paper sheet and historical paper from a Dutch landownership document dated 1834. The viscose fibres were purchased in bundles, from which an individual fibre could be released in a relatively simple fashion. The tested viscose fibre is a Leonardo viscose fibre from Kelheim Fibres, and is characterised by a flat, rectangular cross-section, see also Fig. 1b.

The fibre was subsequently attached to a small frame that was cut out from a 0.5 mm-thick PMMA (Polymethylmethacrylate) sheet using a laser cutter. The frame construction departed from the procedure originally proposed by Jajcinovic et al. (2016),

with some modifications applied, as summarized in Maraghechi et al. (2021) and explained in detail in the following. The frame contained a central window of a width of approximately $800\ \mu\text{m}$ that defines the gauge length, and two side bridges with a height of approximately $500\ \mu\text{m}$, see Fig. 2. Prior to testing, the two bridges prevented the fibre from being loaded, and avoided the occurrence of irreversible deformations or damage, as may happen during cross-sectional measurements, the application of the speckle pattern for digital image correlation (DIC), or the placement of the frame in the tensile tester. At the start of the tensile test, the two side bridges were cut, so that the applied tensile load could be fully transferred to the fibre. Different from the approach of Jajcinovic et al. (2016), a small, longitudinal slit was made at the centre of the frame, which, during placement and alignment of the fibre, guarantees that the line of action of the applied tensile load coincides with the longitudinal direction of the fibre. Nail polish was used for glueing the fibre to the frame, which was done by placing one droplet and aligning the fibre at one end using fine-tip tweezers. Subsequently, another droplet of nail polish was placed to put the other end of the fibre in place, after which the glue was allowed to cure for a minimum period of 24 hours.

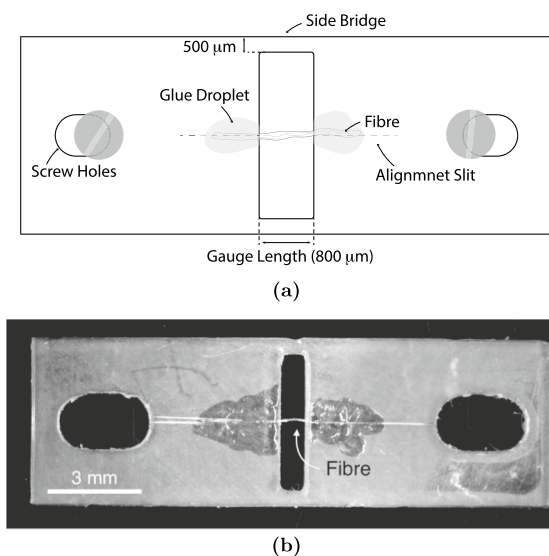


Fig. 2 A cellulose fibre attached to a laser-cut PMMA frame that maintains the fibre integrity prior to testing. **a** Schematic representation. **b** Photograph of the specimen

It is noted that the outer surface of organically-formed cellulose fibres is commonly characterized by the presence of particles, fibrils or fragments from other fibres, which can influence the quality of the applied speckle pattern required for GDHC. Hence, after attaching the fibre to the frame, the fibre was cleaned gently with a fine soft paint brush to eliminate such residuals. Subsequently, the fibre was ready for cross-sectional measurements and DIC patterning.

In order to attain reliable data from the micro-tensile testing, during the sample preparation procedure a possible twisting of the fibre needed to be limited. This is a challenging task, especially in the case of paper fibres, which may exhibit some natural twist that is difficult to quantify under the microscope due to their translucent nature. In Section Microtensile test it will be demonstrated, however, that the present methodology can be used to accurately evaluate the mechanical response of fibres exhibiting a certain degree of twisting.

Cross-sectional area measurement along the longitudinal fibre direction

The measurement of the cross-sectional area profile along the longitudinal fibre direction was necessary to determine the local fibre stresses. This was not a trivial task, since organically-formed cellulose fibres have a highly irregular shape, with considerable cross-sectional changes from one location to another. In order to account for this aspect, a novel method based on optical profilometry has been developed that measures the cross-sectional area profile of an individual fibre across its entire length. Accordingly, White Light Interferometry (Bruker NPFLEX system) was applied to measure the height profiles (and fibre surface profiles) at the top and bottom sides of the fibre prior to the tensile testing. The cross-sectional area of each section could next be evaluated by adequately positioning these two height profiles with respect to each other. A $20\times$ objective lens with a $2\times$ multiplier was used to capture the images, which facilitated the measurement procedure by providing a sufficiently large working distance. The proper positioning of the two height profiles of each section along the fibre length allowed us to accurately determine the cross-sectional area profile and was performed in accordance with the procedure described below.

of the distance between the top and bottom fibre surfaces, whereby the fibre width was deduced from the image at the top surface. The local cross-sectional area, which was needed for the determination of the local stress, was calculated by multiplying the local width and thickness. Note that for cellulose fibres the surface is transparent and very rough, which resulted in a relatively low signal-to-noise ratio in the height profiles, especially for the bottom surface, due to a limited optical signal from the reflection. Accordingly, to further reduce the noise in the cross-sectional area measurement, smoothing steps with Gaussian filters were applied to the height profiles and to the thickness and width measured along the fibre length. For the viscose fibre the signal-to-noise ratio was higher, due to its smooth surface.

Micro-speckle pattern application for digital image correlation

The local fibre strains were accurately measured by means of DIC, according to the GDHC procedure presented in Section Global Digital Height Correlation analysis. In order to effectively evaluate deformations with DIC, a certain amount of contrast is needed on the top surface of the fibre specimen. In principle, cellulose fibres exhibit a natural surface pattern due to their microstructural morphological features. However, this natural pattern does not provide sufficient surface contrast and also is “unstable”, i.e., the surface profile changes non-uniformly during loading. Therefore, at the top surface of the fibre, a 3D speckle pattern was applied based on spherical polystyrene particles of 1 μm diameter. Specifically, a dilute solution of polystyrene particles was prepared in ethanol (0.5 mg/ml), which needed to be sonicated in a cold water bath for a period of 30 minutes. The solution was then sprayed on the fibres from a 6 cm distance for approximately 10 minutes, using an airbrush with 1 bar pressure. In order to create a uniform speckle pattern on the rough fibre surface, the air circulation around the fibre needed to be kept limited. For this purpose, the empty space of the PMMA frame beneath the fibre was filled with a soft paste-like material, by carefully pushing the frame on a piece of glue pad (Polyisobutylene with inorganic filler). The frame was gently removed from the glue pad after the patterning procedure of the fibre surface was finished. As an example, Fig. 4 shows the speckle

pattern applied on a paper fibre, with Fig. 4a depicting a scanning electron micrograph of a patterned paper fibre and Fig. 4b showing the height profile of a section of a paper fibre.

Micro-tensile test

After the fibre was attached to the PMMA frame and the speckle pattern was applied, the *in-situ* tensile test was ready to be performed. For this purpose, a Kammrath & Weiss micro-tensile stage with a 20 N load cell was used, see Fig. 5. The image acquisition was done using a Bruker NPFLEX optical profilometer with a 100 \times objective lens. In order to make the imaging possible with a small working distance of the objective, two aluminium blocks were fixed to the grips of the tensile stage, to which the PMMA frame was screwed, see the right picture in Fig. 5. Before tightening the screws on the frame, the fibre was inspected under the microscope at a lower magnification, in order to verify that it was oriented parallel to the loading axis. In case of misalignment, the frame was carefully rotated until the fibre was aligned with the tensile stage. The screws were finally tightened and the side bridges were carefully melted away using a soldering iron equipped with a thin metal wire at the tip for achieving accuracy in this process.

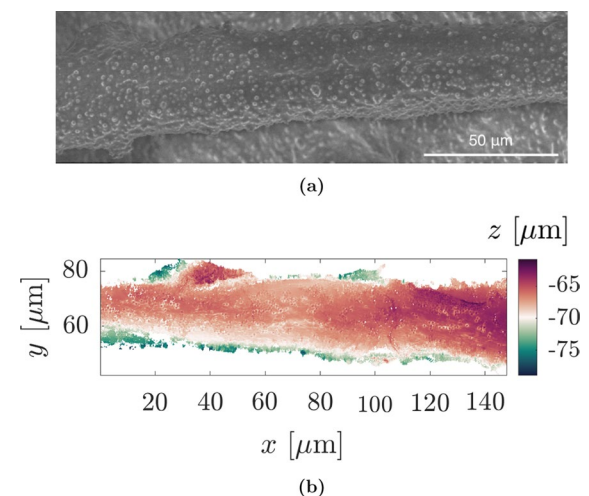
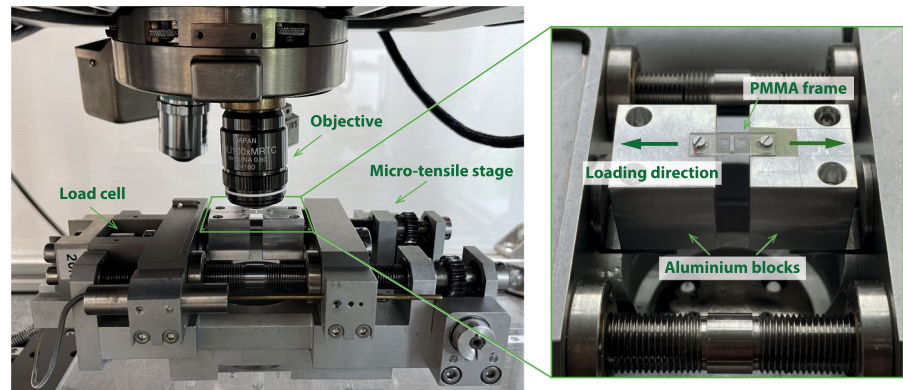


Fig. 4 DIC speckle pattern generated by applying polystyrene particles on the top surface of an organically-formed cellulose (paper) fibre. **a** SEM image, and **b** optical profilometry height profile

Fig. 5 *In-situ* test setup that consists of the micro-tensile stage underneath the optical profilometer. The detailed, right picture illustrates the aluminium blocks that raise the PMMA frame with the fibre specimen, which allows for creating a short working distance for the 100× objective



The tensile test was performed quasi-statically in a displacement-controlled manner, using relatively small, fixed displacement increments, whereby the corresponding force value was measured from the load cell. At each loading step, eight images were taken with a horizontal field of view of 148 μm (100× objective with 0.55× multiplier), which had approximately 50% mutual overlap in the length direction of the fibre. Each of these eight images from hereon is referred to as a *section*. The fibre parts close to the frame were not imaged, since these were (partially) covered by glue. The above procedure resulted in the imaging of 666 μm of fibre length, which corresponded to 83% of the total fibre gauge length of 800 μm (i.e., the width of the window in the PMMA frame). The stepwise load application and image acquisition continued up to failure of the fibre specimen. The acquisition of all the height profiles took between five to ten minutes, during which some stress relaxation occurred due to the viscoelastic behaviour of the fibre, see also Eder et al. (2008); Czibula et al. (2019); Kouko et al. (2019). The force value stored at each loading step corresponded to the value obtained after stress relaxation, i.e., it was recorded right before the application of the next loading step. In order to locally filter noisy data from the height maps, in the profilometry settings a threshold criterion was selected that excludes data points with a noise-to-signal ratio of more than 10%. On the registered fibre surface, the deleted data points appeared as small white spots, see Fig. 4b.

Global digital height correlation analysis

After completion of the test, the local strains in the fibre were evaluated at each loading step from the images obtained by optical profilometry. To this aim, Global Digital Height Correlation (GDHC) was used, which is a full-field displacement measurement method based on the comparison of images of height profiles taken before and after the application of a load increment (Neggers et al. 2014, 2016). GDHC is a modified version of DIC, which specifically enables to evaluate the strain in the presence of out-of-plane displacements, as caused by uncurling and twisting behaviour typically observed in the tensile testing of natural, irregular fibres.

For an accurate comparison of the height profiles with GDHC, every pixel in the reference image is mapped in a second image at its “deformed position”, as taken after the application of the actual load increment. The residual field is defined by

$$r(\mathbf{x}) = f(\mathbf{x}) - g(\mathbf{x} + u(\mathbf{x})\mathbf{e}_x + v(\mathbf{x})\mathbf{e}_y) + w(\mathbf{x}), \quad (2)$$

where \mathbf{x} is the position vector, u and v are the in-plane displacement components in x - and y -directions, respectively, \mathbf{e}_x and \mathbf{e}_y are the orthonormal unit vectors in a Cartesian coordinate system, w is the out-of-plane displacement component in z -direction, and f and g respectively denote the height profiles of the reference and deformed fibre configurations. In order to limit the number of unknowns in the mathematical

formulation, the displacement field is parameterized as

$$\mathbf{u}(\mathbf{x}) \approx \mathbf{u}^*(\mathbf{x}, \underline{\mathbf{a}}) = \sum_{i=1}^n a_i \boldsymbol{\varphi}_i(\mathbf{x}), \quad (3)$$

where $\mathbf{u}(\mathbf{x}) = u(\mathbf{x})\mathbf{e}_x + v(\mathbf{x})\mathbf{e}_y + w(\mathbf{x})\mathbf{e}_z$, with \mathbf{e}_z the unit vector in the z -direction. Further, n is the number of degrees of freedom, $\underline{\mathbf{a}}$ is the vector containing the degrees of freedom $\{a_1, a_2, \dots, a_n\}$, and $\boldsymbol{\varphi}_i(\mathbf{x})$ are appropriate basis functions. In this work, the displacement field of the fibre is parameterized by means of a second-order polynomial basis function for each so-called *region of interest* (ROI) defined in the longitudinal direction of the fibre, with the ROIs illustrated in Fig. 7 by partially overlapping, dashed rectangles. The above choice of basis function defines the strain field within the ROI to be linear, which is considered to be sufficiently accurate as it is expected to be close to homogeneous (as confirmed in Section Micro-tensile test). The optimal set of degrees of freedom that defines the parameterized displacement field $\mathbf{u}^*(\mathbf{x})$ is then calculated by minimizing the square of the residual field r in Eq. (2) with respect to the degrees of freedom a_i assembled in $\underline{\mathbf{a}}$:

$$\underline{\mathbf{a}}^{opt} = \underset{\underline{\mathbf{a}}}{\operatorname{argmin}} \int r^2(\mathbf{x}, \underline{\mathbf{a}}) d\mathbf{x}, \quad (4)$$

in which Eq. (3) has been formally applied. The solution of the above minimization problem is obtained by using an iterative (Newton-Raphson) solution scheme, which subsequently leads to the determination of the displacement field via Eq. (3). The strain tensor is determined with respect to the (non-flat) initial surface, by computing the logarithmic strain values in the two in-plane directions x and y from the corresponding stretch ratios. Note that this initial surface corresponds to the ROI surface in the first, reference image of the pair of images used for the computation of the residual field at each load step, Eq. (2). For more details on the strain calculation procedure, the reader is referred to Shafqat et al. (2018).

The GDHC procedure was performed in an incremental fashion, whereby the incremental strain was calculated from the images taken at two subsequent loading steps. The total strain at the actual loading step was then obtained by adding the incremental strain to the total strain computed at the previous loading step. By updating the strain from two

subsequent loading steps, convergence problems were avoided that may occur when the strain update would have been computed over the *total* elapsed time, by correlating the image at the actual loading step to the reference image taken at the *first* loading step. Such convergence problems are caused by straightening, rotation and out-of-plane deformation of the fibre, as a result of which a correlation of the speckle pattern following from the first reference image and that from an image at a later loading step can not be accurately established. Once the strain fields were computed for all loading steps, the average strain per load step was determined in each ROI, as needed for the construction of the (local) stress-strain curve in the ROI. Recall from the discussion in Section Micro-tensile test that the images represent small regions, in which some of the height data are missing, due to the 10% noise-to-signal filtering threshold that was selected for eliminating noisy data points during data acquisition. Despite the 10% filtering threshold, it was a posteriori noticed that various pixels surrounding the eliminated data were still too noisy, causing convergence problems in the GDHC procedure. In order to overcome this problem, the regions with missing data values were uniformly expanded in the height profiles by eliminating the one layer of pixels located directly along their circumference, which further reduced the influence of local noisy data on the correlation analysis (Vonk et al. 2020, 2021). Subsequently, the average stress in an ROI was calculated from the applied force and the average cross-section of the ROI. Here, the cross-sectional area was determined from the original fibre geometry, i.e., the calculated stress value reflects the engineering stress. From the stress-strain curve in each ROI, the local Young's modulus, the strain at fracture and the ultimate tensile strength were deduced. A comparison of the material parameters obtained for the individual ROIs provides insight into their variation along the fibre length, which will be studied in detail in Section Results and Discussion below.

Results and discussion

The experimental methodology presented in Section Methodology was applied to three different types of fibres. First, a viscose fibre with a flat, rectangular cross-section was tested, i.e., a Leonardo viscose

fibre from Kelheim Fibres. Second, six paper fibres extracted from a Whatman No. 1 filter paper sheet were tested. These fibres exhibit significant intra-fibre and inter-fibre variations in geometry and physical properties, which were exploited to demonstrate the potential of the method for an accurate experimental analysis of organically-formed fibres. Third, two aged paper fibres were tested, which were extracted from an historical Dutch landownership document dated 1834. The test results for aged fibres should provide insight into the suitability of the experimental methodology for the mechanical analysis of fibres taken from valuable and historical objects, for which typically a limited number of samples is available. The measurement results for the viscose fibre, the fibres from Whatman filter paper, and the fibres from the aged paper are respectively discussed in Sections Measurement results for viscose fibre, Measurement results for fibres extracted from Whatman filter paper and Measurement results for fibres extracted from historical paper dated 1834.

Measurement results for viscose fibre

Cross-sectional area

Fig. 6 depicts the results of the cross-sectional area measurement performed on the viscose fibre. The height profiles at the top and bottom surfaces of the fibre are presented in Fig. 6a, and the fibre width and thickness profiles in the longitudinal (x -)direction are illustrated in Fig. 6b and c, respectively. The origins adopted for measuring the height profiles at the top and bottom fibre surfaces are represented by the corresponding scanning centres, as explained in Section Cross-sectional area measurement along the longitudinal fibre direction. It can be confirmed that the width and thickness profiles of the viscose fibre are characterised by relatively small spatial variations, which is in agreement with the regular, uniform fibre shape. The somewhat abrupt change at the right end of the fibre is an edge effect caused by the fibre support, i.e., the glue used for attaching the fibre to the frame. Measurement inaccuracies due to edge effects are avoided by evaluating the stress and strain profiles over a length that excludes the contributions near the left and right edges, as indicated by the two vertical dash-dotted lines in Fig. 6b and c. In the example shown in Fig. 6 this length equals $577 \mu\text{m}$, and from

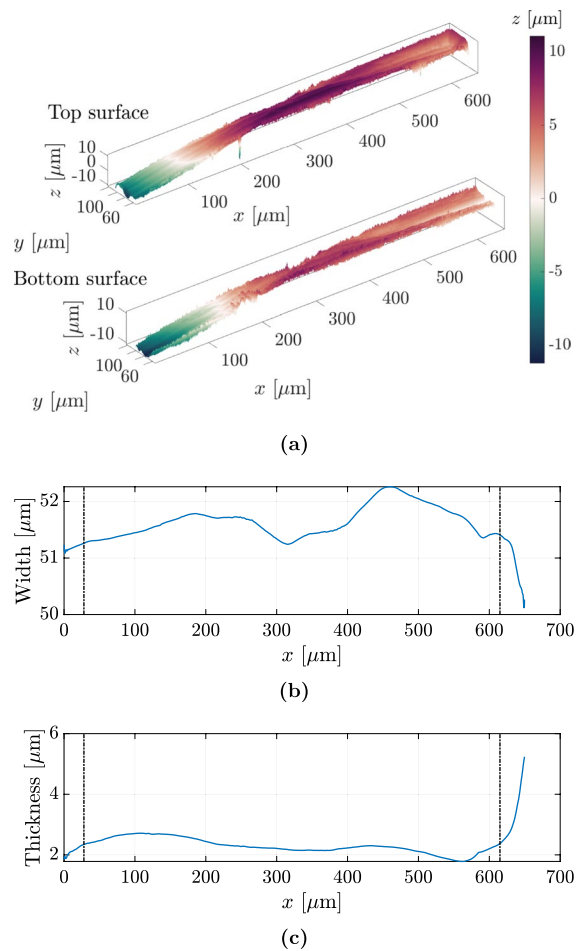


Fig. 6 Results from the experiments performed on the *viscose fibre*. Cross-sectional area measurement illustrating **a** the height profile at the top and bottom surfaces of the fibre, the **b** width profile, and **c** thickness profile, measured in the longitudinal (x -)direction of the fibre. The vertical dash-dotted lines denote the *characterisation range* within which the fibre response is evaluated

hereon will be denoted as the *characterisation range*. Across the characterisation range the average values of the width and thickness of the viscose fibre are $51.7 \mu\text{m}$ and $2.3 \mu\text{m}$, respectively, whereby the corresponding standard deviations indeed remain small, i.e., $0.3 \mu\text{m}$ and $0.2 \mu\text{m}$, as viscose fibres are expected to have a well-defined cross-section.

Micro-tensile test

As discussed in Section Micro-tensile test, at each loading step of the tensile test the height profile is

recorded at a number of sections that partially overlap each other, whereby their specific number depends on the fibre length and is equal to eight for the fibres analysed in this study. This is illustrated in Fig. 7, which shows the overall height profile of the viscose fibre as obtained at the first loading step. The corresponding cross-sectional area profile displayed in this figure is computed by multiplying the width and thickness profiles shown in Figs. 6b and c, respectively. The overlapping, dashed rectangles depicted on each of the eight sections illustrate the ROIs within which the strain is evaluated by means of GDHC. The vertical dash-dotted lines denote the characterisation range, of which the size coincides with the outer boundaries of the first and last ROI. The maximum number of ROIs within a section equals three and is set by the quality of the height profile and the speckle pattern obtained. The total number of ROIs of a fibre straightforwardly follows from summing up the number of ROIs in the eight sections of a fibre. The average number of ROIs per section is typically less than the maximum number of three, as ROIs containing an inadequate strain measurement need to be discarded in the evaluation of the results. An inadequate strain

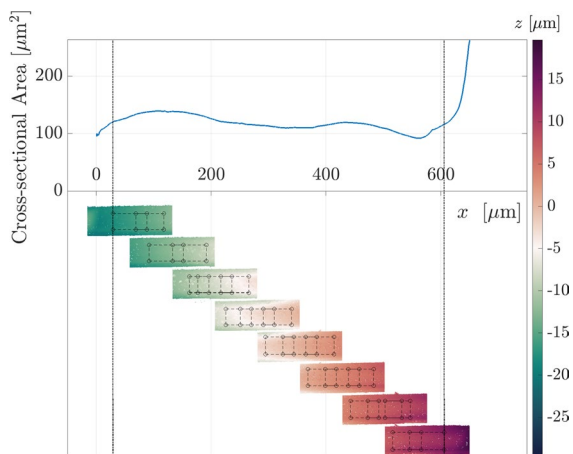


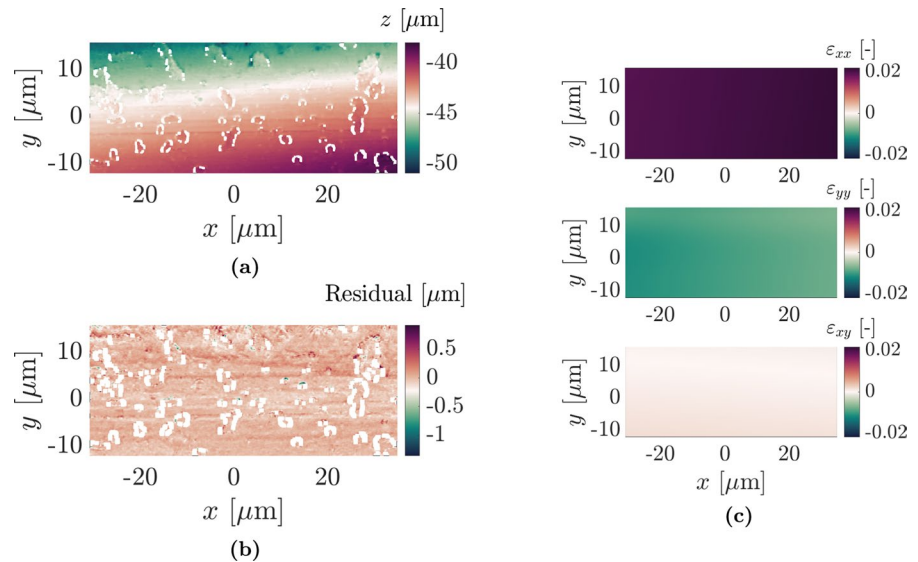
Fig. 7 Results from the experiments performed on the *viscose fibre*. Height profile at eight sections that overlap in the longitudinal (x -)direction of the fibre, as obtained at the first loading step. The displayed cross-sectional profile is computed by multiplying the width and thickness profiles shown in Fig. 6b and c, respectively. The partially overlapping, dashed rectangles within each section illustrate the (two or three) ROIs used for evaluating the strain via GDHC. The vertical dotted lines denote the characterisation range within which the fibre response is evaluated

measurement may result from an inappropriate local speckle pattern, or from a low quality of the local height map due to a rough fibre surface. This latter aspect obviously appears more frequently for irregular, organically-formed fibres than for smooth, regenerated fibres. Accordingly, the total number of ROIs for organically-formed fibres is commonly lower than for regenerated fibres. Note that for the regenerated viscose fibre considered in Fig. 7 the total number of ROIs equals 21, which is indeed relatively close to the maximum number of ROIs of $3(\text{ROIs}) \times 8(\text{sections}) = 24$.

Fig. 8a illustrates the results of the GDHC procedure, as evaluated at one specific ROI at the penultimate step of the loading procedure, i.e., the step before the fibre breaks. Here, Fig. 8a shows the reference height profile that corresponds to the first image from the penultimate loading step, and Fig. 8b presents the residual field, as computed via Eq. (2). The white pixels visible in Fig. 8a represent data points that are deleted due to exceeding the 10% noise-to-signal filter threshold applied during the acquisition of the images, and appear to be located around the circumference of the deposited polystyrene particles of the GDHC speckle pattern. As mentioned in Section Global Digital Height Correlation analysis, the (small) regions with deleted data were uniformly expanded along their circumference by one layer of pixels for further noise reduction, see the discussion in Section Global Digital Height Correlation analysis. This expansion can also be observed in the residual field shown in Fig. 8b, where the areas covered by white pixels are slightly larger than those illustrated in Fig. 8a. The GDHC residual field in Fig. 8b demonstrates a good correlation between the reference and deformed height profiles, as can be concluded from the low residual value (visible in light orange) at the centre of the polystyrene particles.

The area outside the particles reveals the surface roughness of the fibre, as indicated by the horizontal profile lines visible in Fig. 8a. Since the surface roughness pattern only slightly changes with the incremental deformation, it also appears in the residual field depicted in Fig. 8b. The minimization of the square of the residual field $r(\mathbf{x})$, defined by Eq. (4), provides the three-dimensional displacement field $\mathbf{u}(\mathbf{x})$, and thereby the strain field $\boldsymbol{\varepsilon}(\mathbf{x})$. Fig. 8c depicts the three in-plane components of the strain tensor, $\varepsilon_{xx}(\mathbf{x})$, $\varepsilon_{yy}(\mathbf{x})$ and $\varepsilon_{xy}(\mathbf{x})$, which are obtained at the

Fig. 8 Results from the experiments performed on the *viscose fibre*. Global digital height correlation of an individual ROI at the penultimate loading step, showing **a** the reference height profile, **b** the residual field $r(\mathbf{x})$ given by Eq.(2), and **c** the three in-plane components of the strain tensor, $\varepsilon_{xx}(\mathbf{x})$, $\varepsilon_{yy}(\mathbf{x})$ and $\varepsilon_{xy}(\mathbf{x})$



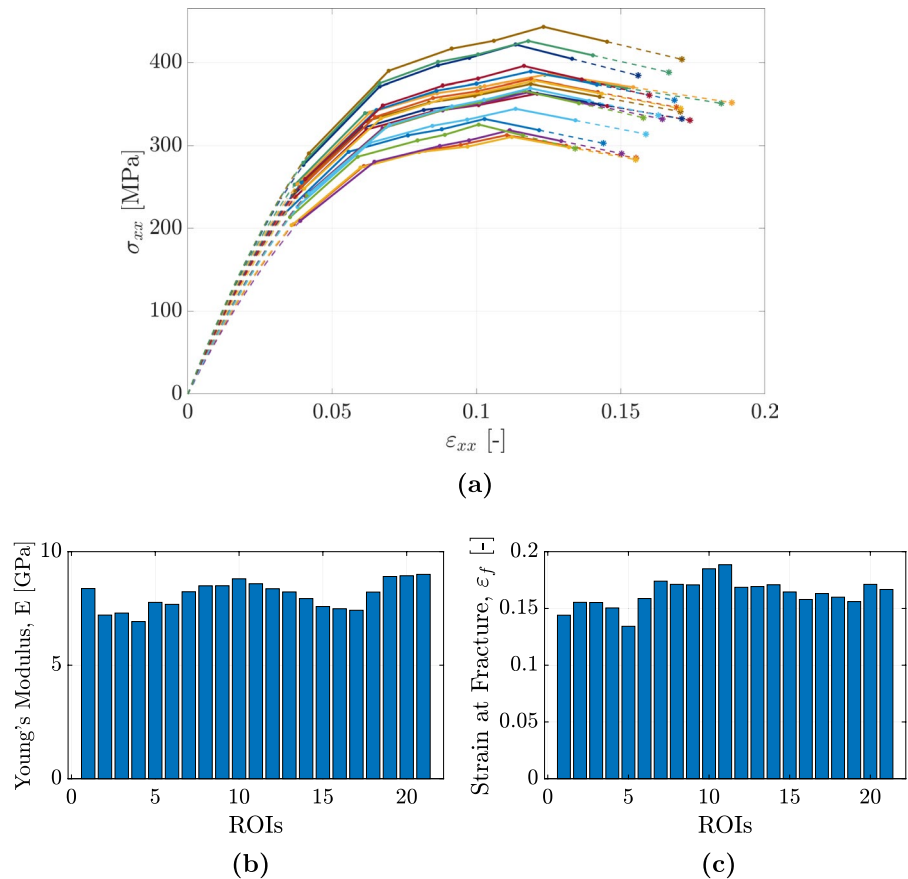
penultimate loading step. Note that the spatial variation of the strain components is negligible across the ROI, i.e., all three strain profiles are approximately homogeneous. Moreover, the small value of the shear strain ε_{xy} confirms that the loading state in the viscose fibre is close to uniaxial tension.

Fig. 9a shows 21 axial stress–strain curves obtained from the different ROIs of the tested viscose fibre. To correct for a small residual stress generated prior to the onset of loading, each stress–strain response is prescribed to start at the origin. Correspondingly, the initial, dashed lines of the curves are anticipated trends obtained by extrapolating the curves to the origin, which is done by fitting a second-order polynomial function through the first three data points of the curves. Observe that the slope of the curves gradually decreases with increasing strain, indicating the development of inelastic deformations caused by micro-damage (local decohesion between microfibrils in case of naturally formed cellulose) and/or micro-plasticity (stretching and relative sliding of polymer chains under alignment/orientation) (Adusumali et al. 2006; Adusumalli et al. 2006; Kouko et al. 2019). After passing the peak stress, the deformation within the fibre starts to localize, whereby the stress decreases with increasing strain, up to the stage at which the fibre breaks. Since fibre fracture occurs at the final loading step, i.e., after the acquisition of the last height map, GDHC can not provide the value of the actual strain at fracture. Accordingly, for each

ROI the strain at fracture is estimated by fitting a first-order polynomial function through the last two data points of the stress–strain curve, up to the final stress value at fracture, as indicated in Fig. 9a by the dashed line at the end of each curve.

The Young's modulus E in each ROI of the viscose fibre is calculated from the initial slope of the corresponding stress–strain curve. The corresponding results are shown in Fig. 9b. The mean value \bar{E} and standard deviation s_E of the Young's modulus over the total number of 21 ROIs are 8.1 GPa and 0.6 GPa, respectively. The average Young's modulus of the viscose fibre is in agreement with other values reported in the literature, which range between 8.3 and 14.0 GPa (Adusumali et al. 2006; Adusumalli et al. 2006; Gindl et al. 2008). In addition, the mean value $\bar{\varepsilon}_f$ and standard deviation s_{ε_f} of the strain at fracture are 0.16 and 0.010, respectively, whereby the mean value falls within the range of values of 0.13 to 0.22 as following from other experimental works (Adusumali et al. 2006; Adusumalli et al. 2006; Gindl et al. 2008). Finally, the fibre tensile strength σ_u is calculated from the ratio between the maximum applied force and the minimum cross-sectional area measured, and equals 467 MPa. This value indeed falls within the range of values of 267 to 471 MPa reported in other experimental works on viscose fibres (Adusumali et al. 2006; Adusumalli et al. 2006; Gindl et al. 2008).

Fig. 9 Results from the uniaxial tensile tests performed on a viscose fibre. **a** Local stress–strain curves obtained from the 21 ROIs along the fibre length. The dashed lines at the beginning and end of each curve reflect anticipated trends and are obtained by extrapolation. **b** Young’s modulus in the individual ROIs. **c** Strain at fracture in the individual ROIs



Measurement results for fibres extracted from Whatman filter paper

Cross-sectional area

The optical profilometry methodology was subsequently applied to six different paper fibre samples, extracted from Whatman No. 1 filter paper. The measurement result of the cross-sectional area profile of one of the fibres is shown in Fig. 10. The height profiles of the top and bottom surfaces of the fibre are depicted in Fig. 10a, while Fig. 10b and c illustrate the width and thickness profiles, respectively. Similar to the viscose fibre, only measurement data within the characterisation range of $581 \mu\text{m}$ are considered. Within this range, the average values of the fibre width and thickness are $27.3 \mu\text{m}$ and $11.1 \mu\text{m}$, and the standard deviations are $2.3 \mu\text{m}$ and $2.2 \mu\text{m}$, respectively. Note that these standard deviations are about one order of magnitude higher than those measured for the viscose fibre as presented above in

Section Cross-sectional area, which obviously is due to the irregular surface profile of the paper fibres. The average width of the six tested fibres varies between $18.3 \mu\text{m}$ and $34.8 \mu\text{m}$, with the standard deviations of the fibre widths ranging between $0.5 \mu\text{m}$ and $2.9 \mu\text{m}$, while the average thickness of the six paper fibres varies between $5.0 \mu\text{m}$ and $11.1 \mu\text{m}$, with standard deviations ranging between $0.9 \mu\text{m}$ and $3.8 \mu\text{m}$. For fibres with a transparent and rough surface, such as cellulose-based paper fibres, the accuracy of the present, local measuring technique is guaranteed for fibres not smaller than those tested in the current study, since otherwise the average signal-to-noise ratio of the height maps may become too low for obtaining useful and accurate measurement results. Conversely, considering the relatively high lateral and vertical resolution of White Light Interferometry, for fibres with a smooth and opaque surface - for which the signal-to-noise ratio of the height maps generally is higher - the minimum fibre size that can be accurately analysed with the present measuring technique

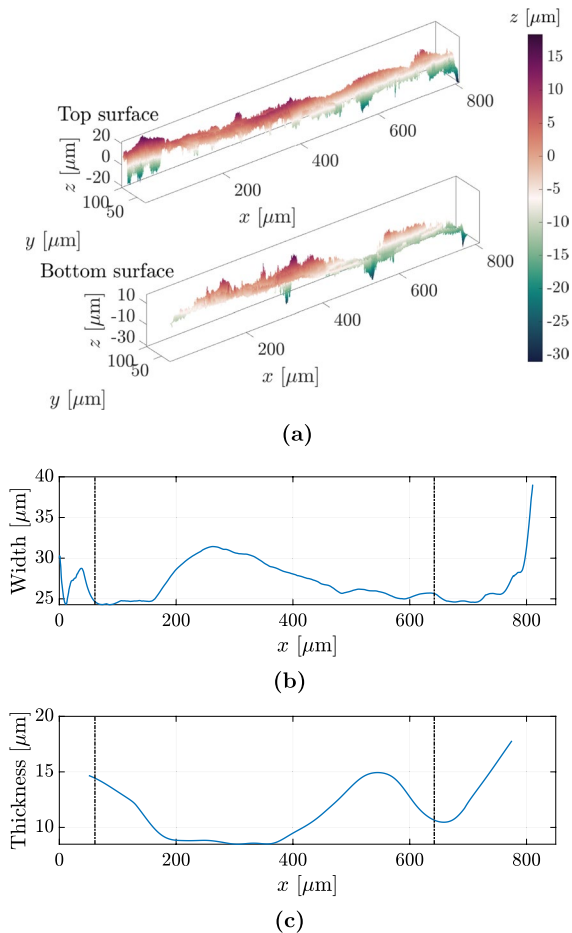


Fig. 10 Results from the experiments performed on fibres from Whatman filter paper. Cross-sectional area measurement of one of the fibres, illustrating **a** the height profiles of the top and bottom surfaces of the fibre, **b** the width profile, and **c** the thickness profile, measured in the longitudinal (x -)direction of the fibre. The vertical dash-dotted lines denote the characterisation range within which the fibre response is evaluated

is expected to lie below that of the fibres tested in the current study.

Micro-tensile test

The tensile stress–strain (σ_{xx} – ε_{xx}) curves obtained in the 11 ROIs of a representative fibre (Fibre 1) are presented in Fig. 11. The paper fibres commonly experience significant uncurling and straightening at the first few loading steps. Hence, the measurements associated with these loading steps were excluded for two reasons. First, due to the considerable rotations and

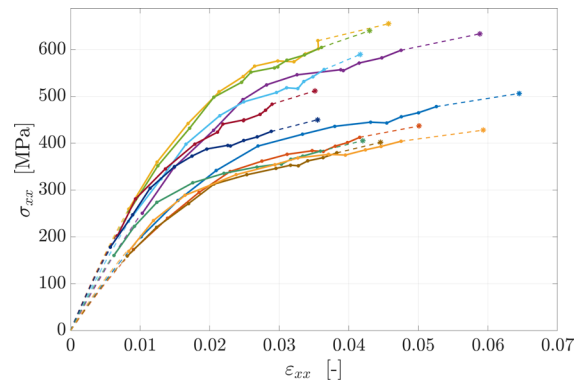


Fig. 11 Results from the uniaxial tensile tests performed on a specific fibre from Whatman filter paper (Fibre 1). Local stress–strain curves obtained from the 11 ROIs along the fibre length. The dashed lines at the beginning and end of each curve reflect anticipated trends and are obtained by extrapolation

out-of-plane displacements, it is difficult to acquire an accurate correlation between the two images taken at a loading step. Second, including possible measurement data from such loading steps may result in an artificial, *increasing slope* of the stress–strain curve, i.e., a stiffening response (Kouko et al. 2019). After the exclusion of these data points, the first part of the stress–strain curve (indicated by a dashed line) is constructed by extrapolating the measurement data towards the origin, using a second-order polynomial function. Further, as already described in Section Micro-tensile test for the viscose fibre, the end of each curve is extrapolated towards the point of fracture by using a first-order polynomial function (indicated by a dashed line). Note that the stress–strain curves show a similar trend as illustrated in Fig. 9a for the viscose fibre; initially, the response is elastic as characterized by a constant slope, which at some stage starts to decrease as a result of the generation of inelastic deformations, until the fibre breaks.

The tensile stress–strain responses of the six tested paper fibres are depicted in Fig. 12, by plotting the minimum (dashed line) and maximum (solid line) responses of the ROIs of each fibre. The labels in the figure refer to the individual fibres, and, for clarity, are used in the discussion below. Observe that the individual fibre responses may be rather different, ranging from relatively stiff (Fibre 2) to relatively compliant (Fibre 4). Further, for all fibres the difference between the minimum and

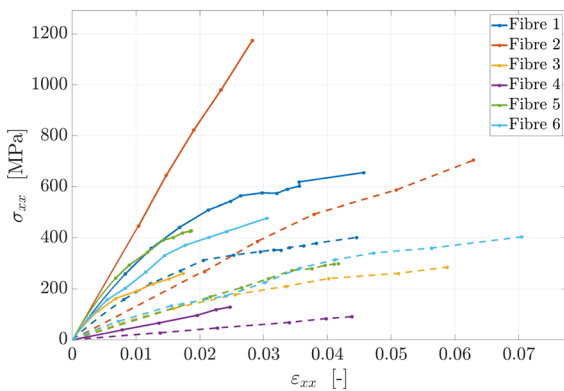


Fig. 12 Results from the uniaxial tensile tests performed on the fibres from Whatman filter paper. The minimum and maximum stress–strain curves in the ROIs of each of the six tested fibres are displayed, as respectively indicated by dashed and solid lines

maximum responses turns out to be significant, suggesting a substantial variation in the local material properties of fibres. This variation is quantified in Fig. 13. Here, Fig. 13a illustrates the value of the Young’s modulus E in the ROIs of the 6 individual fibres, whereby the colours used for distinguishing the fibres correspond to those in the legend of Fig. 12, illustrating that the total number of ROIs differs per fibre. The relatively low number of ROIs for Fibres 1, 4 and 6 is caused by a significant twisting behaviour, as a result of which the local surface speckle pattern required for image correlation at some of the ROIs could not be monitored, so that these ROIs had to be ignored in the data acquisition procedure. Additionally, for Fibre 3 the low number of ROIs is caused by the fact that the surface concentration of polystyrene particles in several ROIs appeared to be too low for a reliable evaluation of the local deformation. The considerable spread in the Young’s modulus measured within each individual fibre and across the different fibres is obviously due to the heterogeneous nature of the organically-formed, cellulose fibres. Fig. 13b illustrates the average Young’s modulus \bar{E} and the standard deviation s_E (indicated by the error bars) for the individual fibres and over the total number of fibres. Here, it is emphasized that the standard deviation over the total number of fibres is computed using the *mean values of all tested fibres* (instead of all ROI values of all tested fibres). Due to the relatively low

number of reliable measurements for Fibre 4 (i.e., 4 measurements), the statistical data of this fibre has been omitted in the figure. The average Young’s modulus of the individual fibres varies between 13.2 GPa and 29.4 GPa, with standard deviations in the range of 5.8 GPa to 11.8 GPa. Further, the average Young’s modulus and standard deviation over the total number of fibres are 21.6 GPa and 7.3 GPa, respectively, which characterize a range of values that includes almost all average Young’s moduli of the individual fibres, see Fig. 13b. Note that the spread in the local Young’s modulus of individual fibres is comparable to the spread in the effective Young’s modulus across the fibres, indicating that the present measurement technique is able to adequately account for fibre stiffness variations by taking measurements from only one, or a few cellulose fibre(s). Further, the above values of the average Young’s moduli fall within the range of values of 4.7 to 35.1 GPa as following from other experimental works on cellulose fibres (Lorbach et al. 2014; Kouko et al. 2019).

Fig. 13c shows the average strain at fracture $\bar{\epsilon}_f$ and the corresponding standard deviation s_{ϵ_f} for each of the fibres (again omitting the results for Fibre 4). The location of the catastrophic failure crack varied per fibre, and could not always be traced accurately, due to its development outside any of the ROIs. Since the fracture data is relatively insensitive to the occasional, initial twisting of fibres, Fig. 13c has been constructed by using the measurement results from *all* ROIs of the fibres. Observe that for the individual fibres the average strain at fracture varies between 0.033 and 0.053, with the standard deviation ranging from 0.010 to 0.023. These values indicate that the strain profile at fracture is rather non-uniform, as caused by geometrical and material heterogeneities in the longitudinal fibre direction. Additionally, the average strain at fracture and corresponding standard deviation over the total number of fibres are 0.042 and 0.008, respectively. The above values for the average strain at fracture fall within the range of values of 0.02 to 0.34 as found in other experimental works on cellulose fibres (Lorbach et al. 2014; Kouko et al. 2019). However, the literature values were generally obtained in a different fashion, namely by determining the *global* fibre strain from the relative

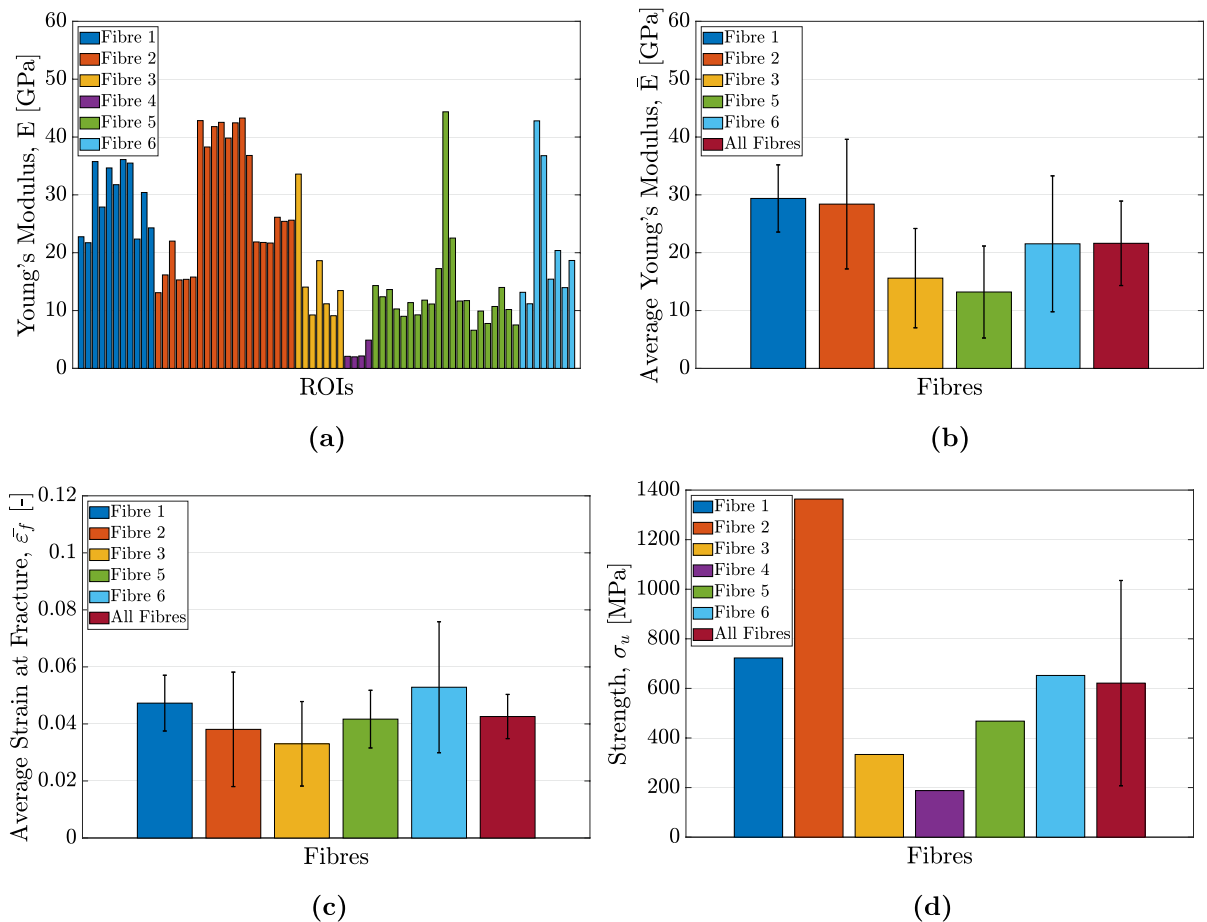


Fig. 13 Results from the uniaxial tensile tests performed on the fibres from Whatman filter paper. (a) Young's moduli E evaluated from the ROIs of the six tested fibres. (b) Average Young's modulus \bar{E} of each fibre, computed as the average of the values from the ROIs. The error bars indicate the standard deviation s_E . The rightmost (crimson red) bar shows the average Young's modulus over the five tested fibres, together with the corresponding standard deviation. (c) Average strain at fracture $\bar{\epsilon}_f$ of each fibre, computed as the average of the values

from the ROIs, with the standard deviation s_{ϵ_f} indicated by the error bars. The rightmost (crimson red) bar shows the average fracture strain over the five tested fibres. Note that Fibre 4 is excluded from the statistical analysis and thus is not included in graphs (b) and (c). (d) Strength σ_u of each fibre, where the rightmost (crimson red) bar shows the average strength value over the six tested fibres, together with the corresponding standard deviation

displacement measured across the tensile stage, which may inadvertently account for fibre slip at the grip surfaces. The present experimental technique excludes this effect by evaluating fibre strains with GDHC locally on the specimen, which may explain why the strain values at fracture on average are lower than those reported in the literature. The stress-strain responses resulting from measuring local and global strains are quantitatively compared in more detail in Section Measurement results for

fibres extracted from historical paper dated 1834 for two fibres extracted from aged, historical paper.

Fig. 13d depicts the tensile strength σ_u of the six tested fibres, which is calculated as the ratio between the maximum force registered during the tensile test and the minimum cross-sectional area of the fibre. Additionally, the average tensile strength of the six fibres is illustrated by the crimson red coloured bar, and equals $\sigma_u = 621$ MPa, with the corresponding standard deviation being 432 MPa. In all but one fibre

(i.e., Fibre 4) localized fracture occurred in the close vicinity of the section characterized by the minimum cross-sectional area, which confirms the correctness of the determination of the tensile strength. Further, the fibre strength values depicted in Fig. 13d turn out to be in good correspondence with the strength values of 330 to 970 MPa reported in other experimental works (Kouko et al. 2019).

Measurement results for fibres extracted from historical paper dated 1834

Micro-tensile test

The proposed measurement methodology has been finally applied to the analysis of two fibres extracted from a historic paper document dated 1834. The cross-sectional measurements of these fibres are similar to those presented in Section Cross-sectional area for Whatman paper fibres and are omitted here for brevity. The local strain evaluations of the two fibres are performed within 13 (Aged Fibre 1) and 10 (Aged Fibre 2) ROIs, and the corresponding stress–strain responses are depicted in Fig. 14 by the blue and light brown solid lines, respectively. In addition, the global stress–strain curves of the two fibres are designated by the corresponding dash-dotted lines. Here, the global strain is determined from the ratio between

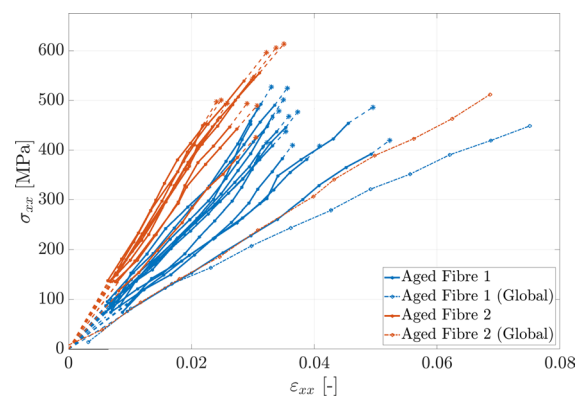


Fig. 14 Results from the uniaxial tensile tests performed on the fibres from aged, historical paper dated 1834. The solid lines represent the local stress–strain curves evaluated from the ROIs of two naturally-aged, historic paper fibres. The dashed lines at the beginning and end of each curve reflect anticipated trends, and are obtained by extrapolation. The two dash-dotted curves represent the global stress–strain curves of the two fibres

the overall displacement measured across the tensile stage (using an LVDT) and the fibre gauge length of $767 \mu\text{m}$, and the global stress follows from the ratio between the force recorded by the load cell and the average cross-sectional area over the actual fibre characterisation range (see Fig. 6). Observe that both the local and global stress–strain curves of the aged fibres are characterised by a linear, elastic branch, up to the point of abrupt fracture. The brittle failure response may be ascribed to fibre embrittlement caused by aging processes (Zou et al. 1994), and clearly differs from the tensile responses of the unaged, viscose fibre (Fig. 9) and the unaged fibres from the Whatman filter paper (Figs. 11 and 12) that are characterized by a gradually decreasing stiffness due to micro-damage and/or micro-plasticity effects before catastrophic failure. As for the unaged fibres, the spread in the local responses of the two aged fibres is considerable, due to their heterogeneous nature. Note further from Fig. 14 that the global responses of the two fibres are characterized by a substantially lower elastic modulus and higher strain at fracture than the local responses, i.e., up to more than a factor of two, which is caused by an overestimated, global deformation that likely results from inadvertently accounting for fibre slip at the grip surfaces. It may therefore be concluded that global stress–strain curves obtained from uniaxial tensile tests on fibres generally should be treated with caution. Furthermore, the experimental data obtained with the present, local measuring method may be significantly more accurate than the data obtained by a common, global measuring method.

From the stress–strain curves in Fig. 14 the mechanical properties of the two aged fibres have been deduced, which are summarized in Fig. 15. The Young’s moduli E measured in the ROIs of the two aged fibres are shown in Fig. 15a, indicating that the spread in the local moduli of the two fibres is comparable, but that the average Young’s modulus \bar{E} of Aged Fibre 1 is lower than that of Aged Fibre 2. This difference is quantified in Fig. 15b, showing that the average Young’s modulus \bar{E} and corresponding standard deviation s_E of Aged Fibre 1 are 11.7 GPa and 2.1 GPa, and of Aged Fibre 2 are 18.4 GPa and 2.1 GPa. Accordingly, the average Young’s modulus across the two fibres equals 15.0 GPa, as indicated by the yellow bar in this figure. Additionally, the average strain at fracture $\bar{\epsilon}_f$ and corresponding standard deviation s_{ϵ_f} for Aged Fibre 1 are 0.038 and 0.006, and for

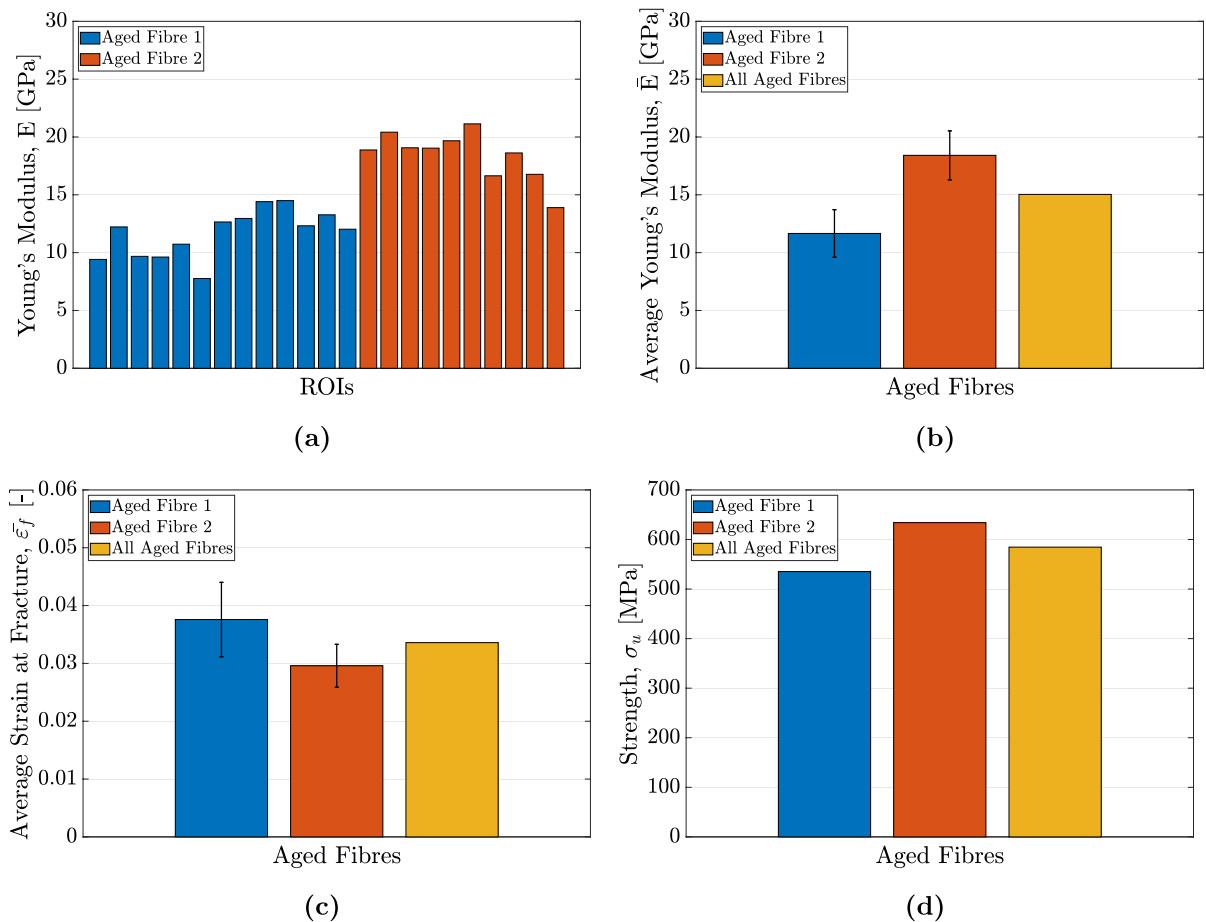


Fig. 15 Results from the uniaxial tensile tests performed on the fibres extracted from aged paper dated 1834. **a** Young's moduli E evaluated from the ROIs of the two aged paper fibres tested. **b** Average Young's modulus \bar{E} of each fibre, computed as the average of the values from the ROIs. The error bars indicate the standard deviation s_E . The rightmost (yellow) bar shows the average Young's modulus over the two tested fibres.

Aged Fibre 2 are 0.030 and 0.004, respectively, leading to an average strain at fracture over the two fibres of 0.034, see Fig. 15c. Finally, the ultimate tensile strength σ_u of Aged Fibres 1 and 2 are 535 MPa and 634 MPa, respectively, in correspondence with an average value over the two fibres of 585 MPa, see Fig. 15d.

Comparison of mechanical properties and failure pattern of the three fibre types

In order to compare the mechanical performance of the aged paper fibres, the (unaged) Whatman paper

c Average strain at fracture $\bar{\epsilon}_f$ of each fibre, computed as the average of the values from the ROIs, with the standard deviation s_{ϵ_f} indicated by the error bars. The rightmost (yellow) bar shows the average fracture strain over the two tested fibres. **d** Strength σ_u of each fibre, where the rightmost (yellow) bar shows the average strength value over the two tested fibres

fibres and the viscose fibre in more detail, for each of the three fibre types, the average mechanical properties over the number of tested fibres are summarized in Table 1. Since for the Whatman paper fibre the number of fibres tested was sufficiently large for obtaining a statistically representative standard deviation, this value is also listed in the table. Although the number of tests used for determining the average properties is different for the three types of fibres, the overview in Table 1 nevertheless points out some interesting features. Specifically, the viscose fibre has a Young's modulus that is a factor of 2.7 lower than that of the Whatman paper fibre, and a factor of 1.9

Table 1 Overview of the average mechanical properties (Young's modulus \bar{E} , strain at fracture $\bar{\epsilon}_f$, and ultimate tensile strength σ_u) of the three types of fibres tested (viscose fibre, Whatman paper fibre and aged paper fibre). For the Whatman

paper fibre the number of tested fibres was sufficiently large for computing a (statistically representative) standard deviation, see also Fig. 13, which is also listed in the table

	Viscose fibre	Whatman paper fibre	Aged paper fibre
Average young's modulus, \bar{E} [GPa]	8.1	21.63 ± 7.3	15.0
Average strain at fracture, $\bar{\epsilon}_f$ [-]	0.160	0.042 ± 0.008	0.034
Ultimate tensile strength, σ_u [MPa]	467	621 ± 432	585

Table 2 Overview of the standard deviations (SD) of the local Young's modulus s_E and local strain at fracture s_{ϵ_f} within

individual fibres of the three fibre types tested (viscose fibre, Whatman paper fibre and aged paper fibre)

	Viscose fibre	Whatman paper fibre	Aged paper fibre
SD Young's Modulus, s_E [GPa]	0.6	5.8 – 11.8	2.1
SD strain at fracture, s_{ϵ_f} [-]	0.010	0.010 – 0.023	0.004 – 0.006

lower than that of the aged paper fibre. Furthermore, its ultimate tensile strength is about a factor of 1.3 lower than that of the other two types of fibres, while its average strain at fracture is more than a factor of 4 higher. Hence, the viscose fibre is characterised by a relatively low strength and stiffness, and a large deformation capacity.

When comparing the average properties of the aged paper fibre to those of the (unaged) Whatman paper fibre, it follows that all three mechanical parameters of the aged paper fibre have lower values, i.e., the Young's modulus, strain at fracture and ultimate tensile strength are, respectively, a factor of 1.4, 1.2 and 1.1 lower. Again, the mechanism of fibre embrittlement by ageing may (to some extent) explain why the aged paper fibre overall has a lower mechanical performance than the Whatman paper fibre.

For a detailed comparison of the spreads measured in the local Young's moduli E and local strains at fracture ϵ_f within individual fibres of the three different fibre types, Table 2 summarizes the values of the corresponding standard deviations s_E and s_{ϵ_f} , as reported previously in Sections Measurement results for viscose fibre to Measurement results for fibres extracted from historical paper dated 1834. Recall that for the viscose fibre only one fibre was tested, corresponding to listing one value for each of the two standard deviations (instead of a range of

values). The table shows that the standard deviation s_E of the Young's modulus of the viscose fibre is a factor of 3.5 *smaller* than that of the aged paper fibre, and on average a factor of 15 *smaller* than that of the Whatman paper fibre. The higher spread in the Young's moduli of the Whatman paper fibre and aged paper fibre compared to that of the viscose fibre is likely due to the irregular shape typical of organically-formed paper fibres, see also Fig. 1. Surprisingly, this feature does not increase the spread measured in the local strains at fracture; instead, the value of s_{ϵ_f} for the smooth, viscose fibre is about a factor of two *larger* than for the irregular, aged paper fibre. This result may be caused by the essentially different fracture responses, which are relatively ductile for the viscose fibre and brittle for the aged paper fibre, see Figs. 9a and 14, respectively.

For obtaining more insight into the differences in fracture behaviour, the top view of the catastrophic fracture pattern of the three fibre types is displayed in Fig. 16. The viscose fibre depicted in Fig. 16a shows a failure crack that is approximately perpendicular to the loading direction. Conversely, for the Whatman paper fibre depicted in Fig. 16b, cracks between individual fibrils develop in the longitudinal fibre direction, whereby catastrophic failure is reached once these longitudinal cracks coalesce

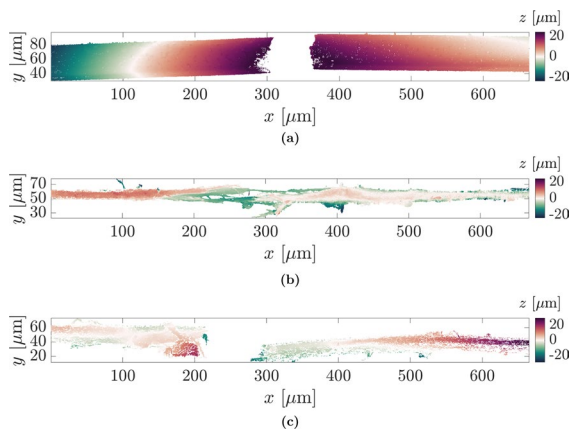


Fig. 16 Top view of the catastrophic fracture pattern of **a** the viscose fibre, **b** a Whatman paper fibre (Fibre 6), and **c** an aged paper fibre (Aged Fibre 1)

by subsequent, transverse fibril fractures across the complete fibre thickness. Finally, Fig. 16c shows that the aged paper fibre fails in brittle fashion by means of a single crack that develops approximately perpendicular to the loading direction. Hence, ageing of paper fibres not only changes the characteristics of the tensile stress-strain response - compare Figs. 11 and 14, but also the characteristics of the corresponding catastrophic fracture pattern - compare Fig. 16b and c.

Conclusions

This paper proposes a novel experimental methodology to measure the mechanical properties of individual fibres of micrometric length, which is based on a combination of *in-situ* micro-tensile testing and optical profilometry. In order to accurately measure the fibre cross-sectional area, optical profilometry is executed at the top and bottom surfaces of the fibre specimen. The local stress is incrementally measured at specific fibre locations from the force value recorded during the tensile test and the local cross-sectional area. By acquisition of height profiles during the micro-tensile testing, in combination with Global Digital Height Correlation (GDHC) a rigorous measurement of local strains at multiple locations along the fibre length is obtained. From the local stress-strain curves, the local Young's moduli, strains at fracture and ultimate tensile strengths are deduced.

The methodology has been applied to three different types of cellulose fibres, i.e., a viscose fibre, fibres extracted from Whatman No. 1 filter paper, and fibres extracted from a historic paper document dated 1834. The main conclusions of the research are listed below.

- The mean value and standard deviation of the fibre width and thickness can be accurately determined by optical profilometry. For the paper fibres, the standard deviation for both the width and thickness may be one order of magnitude higher than those of the viscose fibre, which is due to their irregular surface profile.
- The combination of *in-situ* tensile testing and optical profilometry allows to accurately measure local Young's moduli, strains at fracture and tensile strengths along the fibre length, from which subsequently the effective values of these parameters and their standard deviations can be deduced.
- The spread in the local Young's modulus of individual paper fibres appears to be comparable to the spread in the effective Young's modulus across paper fibres, see Fig. 13b, indicating that the measurement technique is able to adequately account for fibre stiffness variations by performing measurements on just one, or a few, cellulose fibre(s). This makes the experimental methodology very suitable for the mechanical analysis of fibres taken from valuable and historical objects, for which typically a limited number of samples is available.
- As demonstrated for aged paper fibres, the *global* responses of paper fibres are characterized by a substantially lower elastic modulus and higher strain at fracture than the *local* responses, i.e., up to more than a factor of two, see Fig. 14, which is caused by an overestimated, global deformation that likely results from inadvertently accounting for fibre slip at the grip surfaces. Hence, global stress-strain curves deduced from uniaxial tensile tests on fibres should be treated with caution. In addition, the experimental data obtained with the present, local measuring method may thus be significantly more accurate than the data obtained by a common, global measuring method.
- If a fibre is twisted, the local measurement of strain and cross-sectional area can still be carried out accurately for those fibre sections that experience limited twisting. Hence, the test does not

need to be discarded, as would be the case when the strain and cross-sectional area were determined from a global measurement method.

- The aged paper fibre has a lower Young's modulus, strain at fracture and tensile strength than the unaged Whatman paper fibre. The mechanism of fibre embrittlement by ageing may (to some extent) explain the lower mechanical performance of the aged paper fibre, see Table 1. As further indicated in this table, in comparison to the paper fibres, the viscose fibre is characterised by a lower tensile strength and Young's modulus, and a larger strain at fracture.
- The local Young's moduli within the Whatman paper fibre and aged paper fibre show a larger spread than those within the viscose fibre, see Table 2, which is likely due to the irregular shape typical of organically-formed paper fibres, see Fig. 1. Conversely, the spread in the local strains at fracture within the irregular, aged paper fibre is about a factor of two smaller than for the smooth, viscose fibre. This result may be caused by the essentially different fracture response, which is relatively ductile for the viscose fibre and brittle for the aged paper fibre, see Figs. 9a and 14, respectively.

Acknowledgments The authors would like to thank Het Erfgoedhuis Eindhoven, especially Mr. Dirk Vlasblom, for providing the historical paper sample used in the current study.

Author contributions SM has contributed to the conception and design of the experimental method and has executed the experiments, has contributed to the analysis and interpretation of the data, and has drafted and revised the manuscript. EB has contributed to the conception and design of the experimental method, the interpretation of the data, the funding acquisition, and has revised the manuscript. ASJS has contributed to the conception and design of the experimental method, the interpretation of the data, the funding acquisition, the writing of the manuscript, and has revised the manuscript. JPMH has contributed to the conception and design of the experimental method, the interpretation of the data, and has revised the manuscript.

Funding This project has received funding from the European Union's Horizon 2020 research and innovation programme under grant agreement No. 814624.

Data availability Data will be available upon reasonable request.

Declarations

Conflict of interest The authors declare that they have no competing interests.

Ethical approval and consent to participate Not applicable

Consent for publication All the authors give their consent for the publication of this manuscript.

Open Access This article is licensed under a Creative Commons Attribution 4.0 International License, which permits use, sharing, adaptation, distribution and reproduction in any medium or format, as long as you give appropriate credit to the original author(s) and the source, provide a link to the Creative Commons licence, and indicate if changes were made. The images or other third party material in this article are included in the article's Creative Commons licence, unless indicated otherwise in a credit line to the material. If material is not included in the article's Creative Commons licence and your intended use is not permitted by statutory regulation or exceeds the permitted use, you will need to obtain permission directly from the copyright holder. To view a copy of this licence, visit <http://creativecommons.org/licenses/by/4.0/>.

References

- Adusumali RB, Reifferscheid M, Weber H, et al. (2006) Mechanical properties of regenerated cellulose fibres for composites. In: *Macromolecular symposia*, Wiley Online Library, pp 119–125
- Adusumalli RB, Müller U, Weber H, et al. (2006) Tensile testing of single regenerated cellulose fibres. In: *Macromolecular Symposia*, Wiley Online Library, pp 83–88
- Baley C (2002) Analysis of the flax fibres tensile behaviour and analysis of the tensile stiffness increase. *Compos Part A Appl Sci* 33(7):939–948
- Bos HL, Donald AM (1999) In situ ESEM study of the deformation of elementary flax fibres. *J Mater Sci* 34(13):3029–3034
- Burgert I, Frühmann K, Keckes J et al (2003) Microtensile testing of wood fibers combined with video extensometry for efficient strain detection. *Holzforschung* 57(6):661–664
- Čabalová I, Kačík F, Gojny J et al (2017) Changes in the chemical and physical properties of paper documents due to natural ageing. *BioResources* 12(2):2618–2634
- Chen J (2015) Synthetic textile fibers: regenerated cellulose fibers. In: *Textiles and Fashion*. Elsevier, pp 79–95
- Czibula C, Ganser C, Seidlhofer T et al (2019) Transverse viscoelastic properties of pulp fibers investigated with an atomic force microscopy method. *J Mater Sci* 54(17):11448–11461
- Czibula C, Brandberg A, Cordill MJ, et al. (2020) Estimation of the in-situ elastic constants of wood pulp fibers in freely dried paper via AFM experiments. *arXiv preprint arXiv:2012.03037*
- Eder M, Stanzl-Tschegg S, Burgert I (2008) The fracture behaviour of single wood fibres is governed by geometrical

- constraints: in-situ ESEM studies on three fibre types. *Wood Sci Technol* 42(8):679–689
- El-Hosseiny F, Page D (1975) The mechanical properties of single wood pulp fibres: theories of strength. *J Fiber Sci Technol* 8(1):21–31
- Elsayad K, Urstöger G, Czibula C et al (2020) Mechanical properties of cellulose fibers measured by Brillouin spectroscopy. *Cellulose* 27(8):4209–4220
- Emsley A, Heywood RJ, Ali M et al (2000) Degradation of cellulosic insulation in power transformers. part 4: effects of ageing on the tensile strength of paper. *IEE Proc-Sci, Measure Technol* 147(6):285–290
- Ganser C, Hirn U, Rohm S et al (2014) AFM nanoindentation of pulp fibers and thin cellulose films at varying relative humidity. *Holzforschung* 68(1):53–60
- Gindl W, Martinschitz KJ, Boesecke P et al (2006) Orientation of cellulose crystallites in regenerated cellulose fibres under tensile and bending loads. *Cellulose* 13(6):621–627
- Gindl W, Reifferscheid M, Adusumalli RB et al (2008) Anisotropy of the modulus of elasticity in regenerated cellulose fibres related to molecular orientation. *Polymer* 49(3):792–799
- Jajcinovic M, Fischer WJ, Hirn U et al (2016) Strength of individual hardwood fibres and fibre to fibre joints. *Cellulose* 23(3):2049–2060
- Jajcinovic M, Fischer WJ, Mautner A et al (2018) Influence of relative humidity on the strength of hardwood and softwood pulp fibres and fibre to fibre joints. *Cellulose* 25(4):2681–2690
- Kappil MO, Mark RE, Perkins RW, et al. (1995) Fiber properties in machine-made paper related to recycling and drying tension. In: Perkins RW (ed) *Mechanics of Cellulosic Materials*, vol 209. American Society of Mechanical Engineers, pp 177–194
- Kavkler K, Demšar A (2011) Examination of cellulose textile fibres in historical objects by micro-Raman spectroscopy. *SAA* 78(2):740–746
- Kompella MK, Lambros J (2002) Micromechanical characterization of cellulose fibers. *Polym Test* 21(5):523–530
- Kouko J, Jajcinovic M, Fischer W et al (2019) Effect of mechanically induced micro deformations on extensibility and strength of individual softwood pulp fibers and sheets. *Cellulose* 26(3):1995–2012
- Lorbach C, Fischer WJ, Gregorova A et al (2014) Pulp fiber bending stiffness in wet and dry state measured from moment of inertia and modulus of elasticity. *BioResources* 9(3):5511–5528
- Maraghechi S, Bosco E, Hoefnagels JPM et al (2021) An in-depth insight of the mechanical response of cellulose fibres by means of optical profilometry techniques. In: *Optics for Arts, Architecture, and Archaeology VIII*, International Society for Optics and Photonics, 1178415
- Maraghechi S, Dupont AL, Cardinaels R et al (2023) Assessing rheometry for measuring the viscosity-average degree of polymerisation of cellulose in paper degradation studies. *Herit Sci* 11(15):1–9
- Mohanty A, Misra M et al (2000) Biofibres, biodegradable polymers and biocomposites: an overview. *Macromol Mater Eng* 276(1):1–24
- Mott L, Shaler SM, Groom LH (1996) A technique to measure strain distributions in single wood pulp fibers. *Wood Fiber Sci* 28(4):429–437
- Nechyporchuk O, Kolman K, Oriola M et al (2017) Accelerated ageing of cotton canvas as a model for further consolidation practices. *J Cult Herit* 28:183–187
- Neggens J, Hoefnagels JPM, Hild F et al (2014) Direct stress-strain measurements from bulged membranes using topography image correlation. *Exp Mech* 54(5):717–727
- Neggens J, Blaysat B, Hoefnagels JPM et al (2016) On image gradients in digital image correlation. *Int J Numer Methods Eng* 105(4):243–260
- Oriola M, Možir A, Garside P et al (2014) Looking beneath dali's paint: non-destructive canvas analysis. *Anal Methods* 6(1):86–96
- Parsa Sadr A, Bosco E, Suiker ASJ (2022) Multi-scale model for time-dependent degradation of historic paper artefacts. *Int J Solids Struct* 248(111):609
- Seves A, Sora S, Scicolone G et al (2000) Effect of thermal accelerated ageing on the properties of model canvas paintings. *J Cult Herit* 1(3):315–322
- Shafiqat S, Van der Sluis O, Geers MGD et al (2018) A bulge test based methodology for characterizing ultra-thin buckled membranes. *Thin Solid Films* 660:88–100
- Tétrault J, Dupont AL, Bégin P et al (2013) The impact of volatile compounds released by paper on cellulose degradation in ambient hygrothermal conditions. *Polym Degrad Stab* 98(9):1827–1837
- Vonk NH, Verschuur NAM, Peerlings RHJ et al (2020) Robust and precise identification of the hygro-expansion of single fibers: a full-field fiber topography correlation approach. *Cellulose* 27:6777–6792
- Vonk NH, Geers MGD, Hoefnagels JPM (2021) Full-field hygro-expansion characterization of single softwood and hardwood pulp fibers. *Nord Pulp Pap Res J* 36(1):61–74
- Zou X, Gurnagul N, Uesaka T et al (1994) Accelerated aging of papers of pure cellulose: mechanism of cellulose degradation and paper embrittlement. *Polym Degrad Stab* 43(3):393–402
- Zou X, Uesaka T, Gurnagul N (1996) Prediction of paper permanence by accelerated aging I. kinetic analysis of the aging process. *Cellulose* 3(1):243–267